Comprehensive analysis of earthquake source spectra and swarms in the Salton Trough, California

X. Chen[1] and P. M. Shearer[1]

[1] We study earthquakes within California's Salton Trough from 1981 to 2009 from a precisely relocated catalog. We process the seismic waveforms to isolate source spectra, station spectra and travel-time dependent spectra. The results suggest an average P wave Q of 340, agreeing with previous results indicating relatively high attenuation in the Salton Trough. Stress drops estimated from the source spectra using an empirical Green's function (EGF) method reveal large scatter among individual events but a low median stress drop of 0.56 MPa for the region. The distribution of stress drop after applying a spatial-median filter indicates lower stress drops near geothermal sites. We explore the relationships between seismicity, stress drops and geothermal injection activities. Seismicity within the Salton Trough shows strong spatial clustering, with 20 distinct earthquake swarms with at least 50 events. They can be separated into early-M_{max} and late-M_{max} groups based on the normalized occurrence time of their largest event. These swarms generally have a low skew value of moment release history, ranging from −9 to 3.0. The major temporal difference between the two groups is the excess of seismicity and an inverse power law increase of seismicity before the largest event for the late-M_{max} group. All swarms exhibit spatial migration of seismicity at a statistical significance greater than 85%. A weighted L1-norm inversion of linear migration parameters yields migration velocities from 0.008 to 0.8 km/hour. To explore the influence of fluid injection in geothermal sites, we also model the migration behavior with the diffusion equation, and obtain a hydraulic diffusion coefficient of approximately 0.25 m^2/s for the Salton Sea geothermal site, which is within the range of expected values for a typical geothermal reservoir. The swarms with migration velocities over 0.1 km/hour cannot be explained by the diffusion curve, rather, their velocity is consistent with the propagation velocity of creep and slow slip events. These variations in migration behavior allow us to distinguish among different driving processes.

1. Introduction

[2] The SAF (San Andreas Fault) to IF (Imperial Fault) step-over produces regional extension and block rotation within the Salton Trough. The newly discovered hinge zone by *Brothers et al.* [2009] marks the northern limit of active extension and separates the Salton Sea into two sub-basins. High surface temperatures are found along the southern shoreline of the Salton Sea where a buried spreading center is located and maximum subsidence occurs [*Schmitt and Hulen*, 2008; *Svensen et al.*, 2009; *Brothers et al.*, 2009]. The northern end of the Imperial Fault defines a separate subsidence pull-apart basin, the Mesquite Basin [*Brothers et al.*, 2009]. High seismicity is found within the rapidly subsiding basins, whereas the seismicity in the Brawley seismic zone exhibits a ladder-like pattern consistent with block rotation. There are two major geothermal sites in the study region: the Salton Sea geothermal site (at the southern end of the Salton Sea), and the Brawley geothermal site (within the Brawley Seismic Zone).

[3] Previous studies have noted that this region has lower Brune-type stress drops compared to other areas of California, possibly due to high heat flow [*Shearer et al.*, 2006]. Spatial variations of stress drop may reflect the relative strength of fault zones, for example, in the San Andreas Fault zone lower stress drops are found along the creeping section compared to the locked section [*Allmann and Shearer*, 2007]. In order to accurately estimate stress drops from body-wave spectra, the source spectrum needs to be deconvolved from propagation path effects. This is typically done using the empirical Green's function (EGF) method. The traditional approach of estimating the EGF from nearby smaller earthquakes generally requires these

[1]Scripps Institution of Oceanography, University of California, San Diego, La Jolla, California, USA.
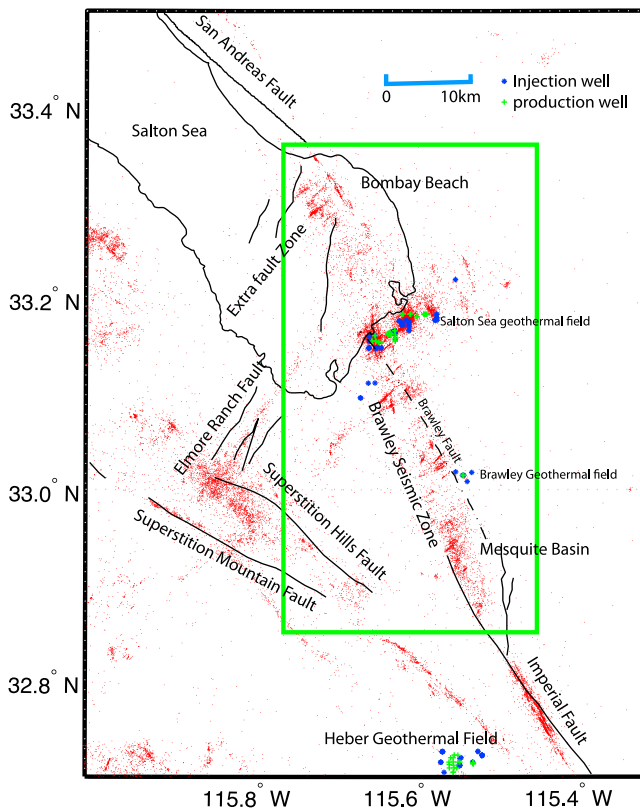
Figure 1. Map view of seismicity from 1981 to 2009 in the Salton Trough. The green box is the study region in this paper. Dashed lines are the estimated Brawley fault location from *Hill et al.* [1975].

events to be at least one magnitude unit smaller than the target event [*Hough and Kanamori*, 2002]. The fact that multiple events are recorded at many stations provides an alternative way to isolate the source spectrum using stacking and a multiple-event EGF method [*Shearer et al.*, 2006]. This method allows us to study both earthquake source parameters and lateral variations in attenuation. Here we extend the *Shearer et al.* [2006] results to a much longer time interval, obtaining stress drop estimates from 1981 to 2009, to study the anomalously low stress drops in the Salton Trough in detail.

[4] Researchers have noted that regions with higher heat flow tend to have more seismic swarms than main shock-aftershock sequences [*Enescu et al.*, 2009] and swarms are often observed in volcanic regions [*Farrell et al.*, 2009; *Fischer*, 2003; *Hayashi and Morita*, 2003]. Most seismic swarms appear driven by an underlying physical change, such as fluid migration or slow slip, and often exhibit spatial migration behavior [*Hayashi and Morita*, 2003; *Lohman and McGuire*, 2007]. A study of the 2000 Vogtland swarm revealed evidence for magma intrusion during the swarm activity from ETAS (epidemic type aftershock sequence) modeling [*Hainzl and Ogata*, 2005]. There have been three well-documented large swarms in 1981, 2005 and 2009 in the Salton Trough. InSar and GPS measurements suggest that the 2005 swarm was driven by aseismic slip along the northeast direction [*Lohman and McGuire*, 2007]. In addition to the three large swarms, there have been many smaller

swarm episodes. Here we analyze the migration behavior for a more complete list of swarms and identify preferred migration directions that appear related to the stress orientation. We also estimate migration velocities, which can be used to estimate hypothetical fluid diffusion rates. These results help to clarify the relationship between the material properties and tectonics in the Salton Trough and its ongoing seismicity.

2. Data and Processing

[5] *Shearer et al.* [2006] studied P wave source spectra for earthquakes in southern California from 1989 to 2001, a period when the seismic network was relatively stable in terms of instrumentation. They obtained stress drop values for over 60,000 events and found spatially coherent patterns in average stress drop, with generally higher values for the eastern Transverse ranges and lower stress drops in the Salton Trough region. In order to make a comprehensive analysis of stress drops in the Salton Trough, we analyze earthquake source spectra for events from 1981 to 2009. We select 14,197 events within our study region (shown by green box in Figure 1) from a precisely relocated catalog (G. Lin, personal communication, 2009) obtained using the method described by *Lin et al.* [2007b]. We then obtain the event waveforms archived at the Southern California Earthquake Data Center, which are filtered to a uniform 100 Hz sampling rate. Displacement spectra are computed with 1.28 s windows starting at the picked P arrival times (operator pick if available, otherwise an autopick). Spectra are selected for analysis that have P wave signal-to-noise ratios (SNR) ≥ 3 for frequency bands of 5 to 10 Hz, 10 to 15 Hz, and 15 to 20 Hz. Event source spectra E_i, station terms S_j and travel-time path spectra $T_{k(i,j)}$ are separated from displacement spectra using the iterative robust-mean method from *Shearer et al.* [2006] using the equation

$$D_{ij} = E_i + S_j + T_{k(i,j)} + R_{ij} \tag{1}$$

At each station, there is usually more than one trace for each component since we use different channels, so we solve for a separate station term for each channel. For the same channel, there might be station term changes during the period from 1981 to 2009 owing to instrumental changes, which often show up as changes in sample rate. We identify systematic changes in resolved parameters from the whole database without considering station term changes and separate them into three periods: 1981 to 1985, 1985 to 1988 and 1988 to 2010. During each period, we find the sample rate for each channel at each station, and solve for a separate station term for each sample rate. We use an iterative robust least squares method [*Shearer et al.*, 2006] to isolate event terms, station terms and travel-time terms. In this processing, we solve for a total of 9397 event terms and 503 station terms.

3. Stress Drop

[6] The stress drop $\Delta\sigma$ can be estimated from the event term E_i. To consider only the best-resolved events, we restrict our analysis to the 3332 events with P wave spectra stacked from at least five different stations that satisfy our SNR criteria. Our computed event terms only provide rel-
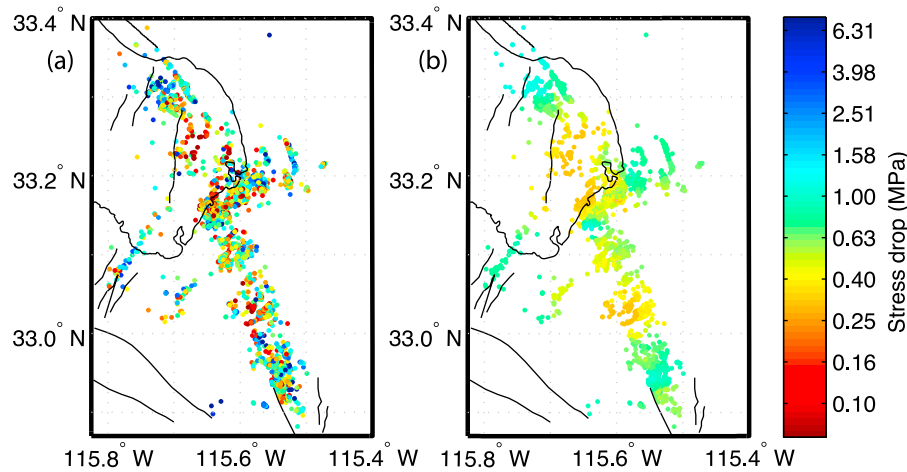
Figure 2. (a) A map view of stress drop estimates for 3332 events obtained using the multiple EGF method. (b) A map view of smoothed stress drop estimates by applying a spatial median filter.

ative spectral shapes among different events and include common path effects that cannot be isolated from travel-time terms. To obtain absolute spectral shapes, we apply the multiple-event empirical Green's function (EGF) method used by *Shearer et al.* [2006] to all of our events. We calibrate the measured relative seismic moment Ω_0 to the absolute moment M_0 using the local magnitude M_L by fitting a linear relationship between $\log(\Omega_0)$ and M_L: $M_L = 1.0 \log_{10}\Omega_0 + 2.19$. We limit our analysis to events with magnitudes lower than 3.5 due to amplitudes "clipping" for larger events.

[7] The source spectra are stacked at 0.2 increments in calibrated-magnitude bins. We first solve for a single regional EGF by fitting a theoretical source model for binned spectra with magnitudes from 1.5 to 2.9, for which all the binned stacked spectra are reasonably smooth. The theoretical spectral model used here was first proposed by *Brune* [1970]:

$$u(f) = \frac{\Omega_0}{1 + (f/f_c)^2} \qquad (2)$$

where Ω_0 is the long-period amplitude and f_c is the corner frequency. The P wave corner frequency f_c can be related to stress drop $\Delta\sigma$ by using the *Madariaga* [1976] relation:

$$f_c = \frac{0.42\beta}{(M_0/\Delta\sigma)^{1/3}} \qquad (3)$$

where β is shear wave velocity (assumed to be 3.5 km/s). We use the method of *Shearer et al.* [2006] to find the best fitting stress drop and the EGF. Next, we correct the individual source spectra by subtracting the EGF, find the best-fitting corner frequency f_c for each event, and compute $\Delta\sigma$ from equation (3). The individual event stress drops exhibit considerable variation but have a median value around 0.5 MPa.

[8] By correcting the event spectra with a single EGF, we are implicitly assuming a uniform attenuation model for the whole region. However, there exists the possibility of lateral variations in material properties which could cause quakes in regions of higher local attenuation than the assumed model to have lower measured corner frequencies and inferred stress drops. For example, *Shearer et al.* [2006] noted that events in the Coso geothermal field have increased stress drops after considering a spatially variable EGF model, and *Allmann and Shearer* [2007] found that an observed temporal variation of stress drops before and after the 2004 Parkfield earthquake can be partially accounted for by a change in attenuation.

[9] In order to test for the effect of possible spatial variations in attenuation, we use a multiple-EGF method to solve for a separate EGF for each individual event using only the closest nearby events. The seismicity is unevenly distributed in this region, with relatively few events near Bombay Beach in the Salton Sea and the Brawley geothermal site, whereas intensive seismicity is found within the Salton Sea geothermal field and the Mesquite Basin region. Considering this difference, we use at least 100 closest neighboring events for each event in the lower seismicity regions, and events within a 2 km radius for each event in the higher seismicity regions. We solve for an EGF for each event using the same procedure as was applied earlier for all events and the same magnitude range. Then the corner frequency and stress drop are calculated from the EGF-corrected source spectrum.

[10] The resulting stress drops after correction for attenuation effects reflect the variations among event source spectra and may indicate the relative strength of fault zones. The individual-event stress drops follow a normal distribution in the log-domain with a median value of 0.56 MPa and values ranging from 0.1 MPa to 3.7 MPa. However, there is a clustering of poorly resolved high stress drops and high corner frequency events, which is probably due to the lower SNR cutoff and the limited frequency band used in the inversion. As in the case of the constant EGF analysis, individual stress drops have considerable variation and we apply the spatial-median filter by finding the median value for 100 closest events to resolve spatial variations in average stress drop (Figure 2b). Note that because of the minimum signal-to-noise criteria for the spectra, stress estimates are obtained for only 25% of the seismicity in the region (3332 out of 14,197 events). We observe spatial variations in median stress drop, with lower stress drops near the
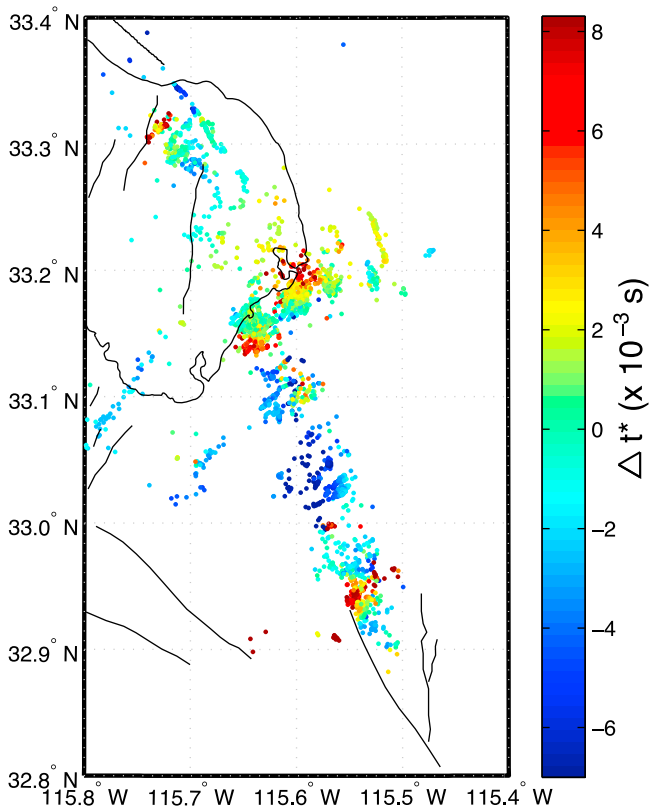
Figure 3. Map view of Δt* variations calculated by a least squares fit to the spectral ratio between the spatially varying EGF and the constant EGF. Colors show Δt* in seconds, with red indicating more attenuation while blue is less attenuation.

southern coast of the Salton Sea and the Brawley geothermal field, whereas higher stress drops are found toward the boundary of the active extension zone. We find that the smoothed spatially coherent pattern is robust regardless of the choice of the number of neighboring events, and thus reflects source property changes among the different regions. The overall distribution of stress drops is much lower than that found for Southern California earthquakes from 1989 to 2001 [*Shearer et al.*, 2006], suggesting relatively weaker fault zones in the Salton Trough. Similar to *Shearer et al.* [2006], we observe no relationship between stress drop and magnitude, suggesting self-similarity among different sized events. We do not observe any clear relationship with depth, probably because the seismicity is confined to a narrow depth zone within each area and any systematic depth variation in stress drop may be masked by larger variations between regions.

4. Attenuation

[11] Using a single EGF, we can compute an average P wave attenuation quality factor (Q_P) for the Salton Trough region from the travel time terms. In order to be consistent with equation (1), we add the computed EGF and the travel-time term to get the true path spectra. We assume that the theoretical spectrum for attenuation is

$$A_k = A_0 e^{-\omega t(k)/2Q_P} \qquad (4)$$

In the log domain, the spectrum has a linear relationship with frequency. A best-fitting Q_P of 340 is found for the Salton Trough region, substantially lower than the average value of 560 found for all of southern California by *Shearer et al.* [2006]. This result is consistent with the high attenuation observed in the Salton Trough region by *Schlotterbeck and Abers* [2001] and *Hauksson and Shearer* [2006].

[12] The difference in results between the new multiple EGF approach and the single EGF method can be related to changes in the attenuation parameter $t*$ (an integrated measure of the attenuation along the raypath: $t* = \int_s Q_P^{-1} dt$). We obtain $\Delta t*$ by least squares fitting to the spectra ratio between the two EGFs in the log domain, a positive $\Delta t*$ indicates an increase in attenuation compared to the regional average. As shown in Figure 3, increased attenuation with $\Delta t*$ of 0.008 s is seen within the newly identified hinge zone within the Salton Sea, the southern coast of the Salton Sea, and the Mesquite Basin, where rapid subsidence and sedimentation is suggested [*Brothers et al.*, 2009]. A crustal tomography map reveals low-velocity anomalies beneath the southern Salton Sea and west of the Imperial Fault at seismogenic depths [*Lin et al.*, 2007a; *Schmitt and Hulen*, 2008], thus higher attenuation in these regions might be expected. Overall, 90% of our observed P wave $\Delta t*$ are from −0.006 to 0.008 s. Using the average travel time of 10 s considered in the travel-time spectra, these variations correspond to Q_P ranging from about 280 to 410, although larger variations are expected for localized anomalies.

5. Geothermal Activities

[13] Relatively lower stress drop values (by approximately 0.12 MPa or about 20% lower than the median) are observed within the geothermal areas, including the southern coast of the Salton Sea and the Brawley geothermal field. The highest seismicity rate in the Salton Trough is seen within the Salton Sea geothermal field where continuous injection and production activities have been conducted since 1982. Injection-induced seismicity has been observed in several geothermal reservoirs in an effort to create an EGS (enhanced geothermal system) to increase the permeability of the material or fluid content [*Gunasekera et al.*, 2003; *Majer et al.*, 2007]. One well-known example is the Geysers geothermal area in northern California. Although the situation in the Salton Sea is different from the HDR (hot-dry-rock) type reservoir of the Geysers [*Majer et al.*, 2007], since the Salton region is already fluid-rich and the injection activities are mainly for water circulation purposes [*Goldsmith*, 1976], the increased pore pressure during injection can trigger earthquakes if the fault zones are near-critical due to reduced effective stress [*Goertz-Allmann et al.*, 2011].

[14] To understand the possible relationship between seismicity and geothermal activities in this region, we focused on a 7 km NE cross-section (see Figures 4 and 5), where about 50% of the total seismicity is located. The cross-section view (Figure 4b) shows that the seismicity clustered into three major separated areas, where each area spans a depth range of about 4 km. The vertical distribution of seismicity is similar to other geothermal sites, i.e., the Geysers [*Ross et al.*, 1999]. The locations of the three clusters correlate with the location of injection wells (see Figure 5), and the initiation of high seismicity coincides with the start of
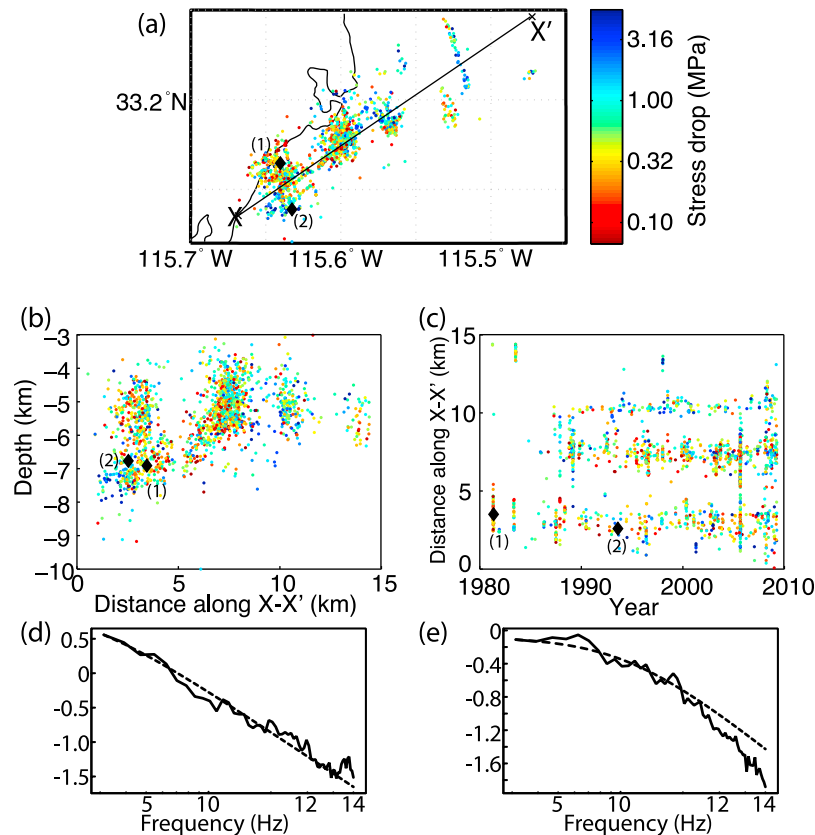
Figure 4. (a) Map view of stress drops near the Salton Sea geothermal site (same region as Figure 5). (b) Cross-section along profile X-X'. (c) Event distance along profile X-X' versus occurrence time and colored by stress drop. (d) Spectrum of a low stress drop event (event 1) with stress drop of 0.12 MPa, corner frequency of 2.8 Hz and magnitude of 2.4. (e) Spectrum for a high stress drop event (event 2) with stress drop of 4.9 MPa, corner frequency of 16 Hz and magnitude of 2.1. The black solid lines in Figures 4d and 4e are EGF-corrected source spectra and the black dashed lines are theoretical spectra. The diamonds in Figures 4a–4c show the locations and times for the two events.

injection activities (see Figures 5b and 5c). It should be noted that Figure 4 only includes events with stress drop estimates, while Figure 5 includes all events with magnitude greater than 1.0, regardless of their stress drop estimates.

[15] To further analyze the relationship between stress drop and distance from geothermal wells, for all events occurring after the start of geothermal activities in the Salton Trough (first record was in 1982), we find the distance to the nearest injection well for each event. We then sort the events according to their distance to the nearest injection wells, and separate them into 10 bins, each with an equal number of events. We find the median stress drop and distance for each bin, and apply a bootstrap method (with resampling) to estimate uncertainties in the median stress drop. Shown in Figure 6, the median stress drop increases with distance from the injection wells to about 2.5 km, a radius which includes about 55% of the events. Beyond 2.5 km, the increasing relationship is not clear, which is probably due to reduced fluid influence at greater distance. Similar relationships have been observed by *Goertz-Allmann et al.* [2011], who found the stress drop increases with pore pressure for up to 300 m within a geothermal reservoir in Switzerland

and suggest that reduced effective stress due to increased pore pressure could explain the relationship.

6. Swarm Activity

[16] Statistical simulations of earthquake clusters using ETAS triggering models [e.g., *Ogata*, 1988] show a higher probability of seismic swarms in regions with higher heat flow and geothermal activities [*Enescu et al.*, 2009]. There have been three major swarms of hundreds of events in the Salton Trough region since 1981. The swarms in 1981 and 2005 were associated with aseismic slip [*Lohman and McGuire*, 2007] and exhibited spatial migration along the cross-section direction (see Figures 7 and 8). The swarms in 1981 and 2005 start with low stress drop events, evolving to higher stress drops near the time of the largest earthquake in the sequence (see Figures 7 and 8). The variation of stress drops within each swarm is similar to the pattern of stress drop increase with distance from geothermal wells.

[17] In addition to the major swarms, there have been a number of smaller swarms in the Salton region, likely promoted by the relatively high flow. To study swarm properties in more detail and possibly relate them to tectonic
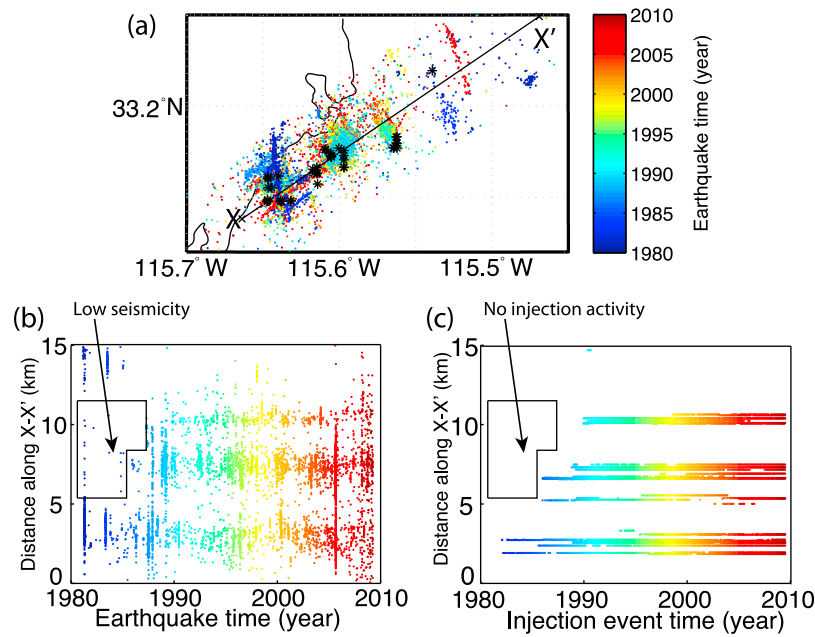
Figure 5. (a) Map view of seismicity near the Salton Sea geothermal site (same region as Figure 4). Events are colored by occurrence time, black stars are locations of injection wells. (b) Event distance along profile X-X′ versus occurrence time. (c) Injection event distance along profile X-X′ versus injection time.

features, we have complied a more complete list of swarms. We begin by searching for seismic 'bursts' using similar criteria as *Vidale and Shearer* [2006], who found 71 seismic bursts in Southern California. We require: (1) there are at least 50 events within a radius of 4 km in 14 days following the initial event; (2) no more than 20% of the events occur between 4 and 8 km from the initial event during the same 14 days; (3) there are fewer than 5 events in the prior 14 days within the same 4 km radius. Using these criteria, we identify 34 seismic bursts, which include some clusters with seismicity distributed within separate distinct areas within the 4 km radius. Visual examination of the spatial and temporal distributions of each burst shows that several bursts are subsets of the 1981 and 2005 swarm groups (the spatial extent and duration of which are beyond our burst selection criteria), and we associate these bursts to the larger swarms. After visual examination, we identify 20 distinct bursts or burst groups. Although in principle, these bursts could include simple main shock-aftershock sequences, we find that all of them exhibit swarm-like behavior to some extent. Thus we will henceforth refer to them simply as swarms rather than bursts, although we recognize that some are more 'swarm-like' than others. The location and time of each swarm is shown in Figure 9. These swarms span two separate periods, from 1981 to 1987 and from 1999 to 2009 (see Figure 9). They tend to cluster in four major regions: near Bombay Beach, the southern shoreline of the Salton Sea, the middle Brawley Seismic Zone, and the northern end of the Imperial Fault. Most of the swarm seismicity is distributed between 0 and 10 km depth, with shallower events in the north and deeper events near the Imperial Fault (see Figure 9b).

6.1. Temporal Behavior

[18] For each swarm, we normalize the time for each event since the beginning of the sequence by the mean time

delay: $t_i = (T_i - T_0)/mean(T_i - T_0, i = 1.N)$. Next we consider the normalized timing of the largest event in the sequence, t_{max}. We classify 6 swarms with $t_{max} \leq 0.4$ as early-M_{max} (more similar to main shock-aftershock sequences) and 14 swarms with $t_{max} \geq 0.6$ as late-M_{max} (more swarm like). We use the skew of moment release history $F(t) = \int_{t_0}^{t} M_0 \, dt$ to further quantify the difference between early-M_{max} and
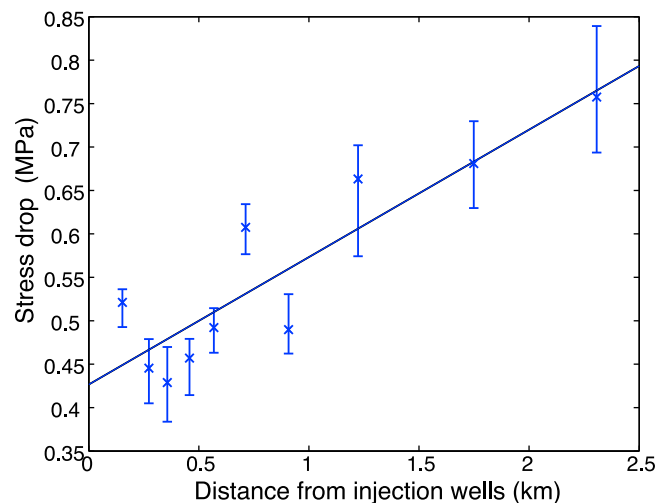
Figure 6. Stress drop versus event distance from the nearest injection wells. The Y axis is the median stress drop for each bin with an equal number of events, sorted by their distance to the injection wells. Error bars are estimated from a bootstrap approach by resampling events within each bin 1000 times, and finding the median value for each resampled data set. The X axis is the median distance from injection wells for events within each bin.
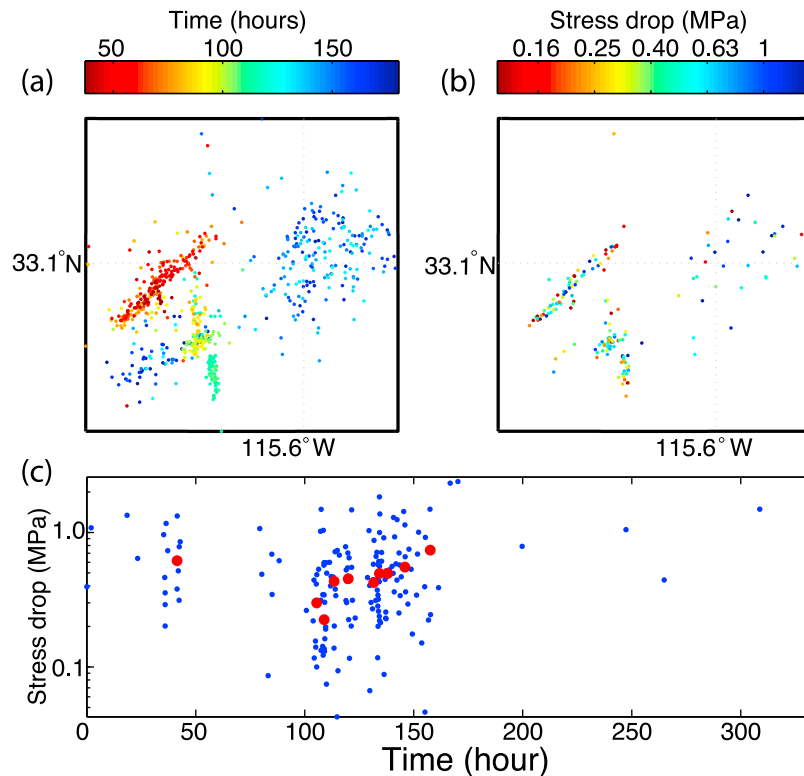
Figure 7. (a) Map view of the 1981 swarm with events colored by their occurrence times. (b) Map view of the 1981 swarm with events colored by their stress drop values. (c) Stress drop versus time for the 1981 swarm. The red dots are median values for 10 bins with an equal number of events.

late-M_{max} swarms. As described by *Roland and McGuire* [2009], a larger positive value is observed for pure aftershock sequences ($t_{max} = 0$) while a lower or even negative value is observed for swarms (which generally have larger t_{max}). For each event, the moment is estimated from the catalog magnitude: $M_0(i) = 10^{(1.5*M_L(i)+9.1)}$ (N-m) [*Kanamori*, 1977]. We do not use the calibrated magnitudes estimated from the spectral analysis because it did not include all the events. The centroid time of moment release is obtained from the weighted mean time: $\bar{t} = \frac{\sum_1^N t_i \times M_0(i)}{\sum_1^N M_0(I)}$.

Individual moment is normalized by $m_0(i) = \frac{M_0(i)}{\sum_1^N M_0(i)}$ so that $F(t \to \infty) = 1$. The third central moment of this sequence is: $\mu_3 = \sum_1^N (t_i - \bar{t})^3 m_0(i)$, the standard deviation: $\sigma = \sqrt{\sum_1^N (t_i - \bar{t})^2 m_0(i)}$. The skew of moment release of each sequence is *skew* = μ_3/σ^3. The skew values for the early-M_{max} group are mostly above 1.8 with one exception at −0.29, the late-M_{max} groups have values between −9 and 1.5, generally lower than the other group. Although the early-M_{max} sequences usually have higher skew values, all the values fall within the range for swarm-like sequences of *Vidale and Shearer* [2006], from −5 to 5 [*Roland and McGuire*, 2009].

[19] Next, we examine the temporal distribution of events by checking the seismicity decay rate. The observed decay rate for most aftershock sequences follows t^{-p}, that is Omori's Law [*Omori*, 1895], where p is typically close to

unity. For each sequence, we compare the time history of seismicity relative to the largest event with $\sim t^{-1}$ predictions. Our results for individual sequences show a variety of patterns that often exhibit a mixture of swarm-like and aftershock-like behavior. To analyze the general features, we stack the seismicity rate within each group according to event time relative to the largest event in each sequence. For the late-M_{max} group, to limit the effect of large sequences, we consider separately the three bursts with more than 400 events and the eleven bursts with fewer than 200 events. Shown in Figure 10, the highest seismicity rate occurred near the time of the largest event, and later seismicity followed a power law decay. The major difference lies in the events before the largest event: the late-M_{max} group (Figures 10a and 10b) has nearly as much seismicity leading up to the largest event as occurs later, while the early-M_{max} group has very few early events and behaves more like a main shock-aftershock sequence. For the three largest swarms, event subclusters occurred about 30 hours before the peak subcluster, and the two subclusters within each burst occurred at different faults due to the large spatial extent of the bursts (Figure 9a).

[20] Figure 10b shows a power law increasing trend of seismicity before the occurrence of the largest event. The post-peak decay is described by Omori's Law; while the pre-peak buildup is sometimes called inverse Omori's Law. Similar temporal distributions are observed for simulated swarm activity based on a self-organization model [*Hainzl*, 2003], and the 2000 Vogtland swarm in Bohemia, which is
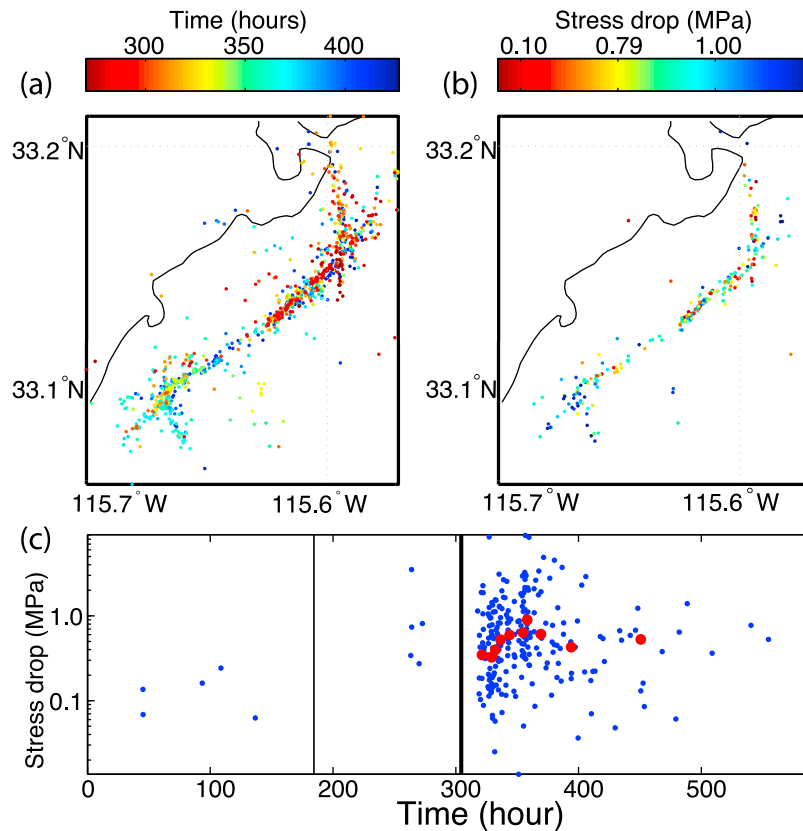
Figure 8. (a) Map view of the August, 2005 swarm with events colored by their occurrence times. (b) Map view of the 2005 swarm with events colored by their stress drop values. (c) Stress drop versus time for the 2005 swarm. The red dots are median values for 10 bins with an equal number of events. The black lines show the occurrence time of injection events within the 2005 swarm region. Thicker line indicates more than 10 injection events occurred around the same time across this region.

suggested to have been triggered by fluid intrusion and driven by post-seismic creep [*Hainzl*, 2004]. Therefore, the temporal distribution of activity indicates there is possible fluid involvement in the triggering mechanism for swarms in the late-M_{max} group.

6.2. Spatial Distribution

[21] Most swarms except the three largest are confined to a narrow region. Following *Vidale and Shearer* [2006], we find the eigenvalues and eigenvectors for the covariance matrix of demeaned hypocentral coordinates of the events within each swarm. For the three large swarms, the events break up into smaller clusters and we use visual inspection to study separately the spatial distribution for each area. The relative sizes of the eigenvalues define the general shape of the cluster, with $\lambda_1 \gg \lambda_2, \lambda_3$ for a linear distribution, $\lambda_1 \approx \lambda_2 \gg \lambda_3$ for a planar distribution, and $\lambda_1 \approx \lambda_2 \approx \lambda_3$ for a spherical distribution. We find that most bursts are linearly distributed along strike, or on a nearly vertical fault plane, while four of them show spherical distributions. Similar to *Vidale and Shearer* [2006], we find that the best fitting planes are mostly near vertical with dip angles ranging from 65° to 89° with the majority greater than 80°. Most smaller swarms are distributed within a narrow depth range of 1 km,

and extend longer distances along strike. General information for each swarm, including its temporal and spatial distribution is listed in Table 1.

6.3. Spatial-Temporal Migration

[22] In an initial visual examination, we plot occurrence time versus distance along strike, and find that all our observed bursts exhibit seismicity migration. This is in contrast to typical main shock-aftershock sequences, which usually do not exhibit spatial migration behavior [*Vidale and Shearer*, 2006], they tend to occur across the entire aftershock region immediately after the main shock. In addition, the magnitude difference between the largest event within even the early-M_{max} group and the next largest event is usually less than 0.3, far lower than the Båth's Law average value of 1.2 [*Båth*, 1965], and the skew values are lower than typical aftershock sequences [*Roland and McGuire*, 2009]. This is why we refer to all 20 of our observed bursts as swarms, rather than aftershock sequences.

[23] In order to quantify swarm migration behavior, we develop a weighted L1-norm method to find the best-fitting migration vector. Observations suggest that the seismicity front is migrating with time, and plots of event time versus distance along the migration direction exhibit an upper tri-
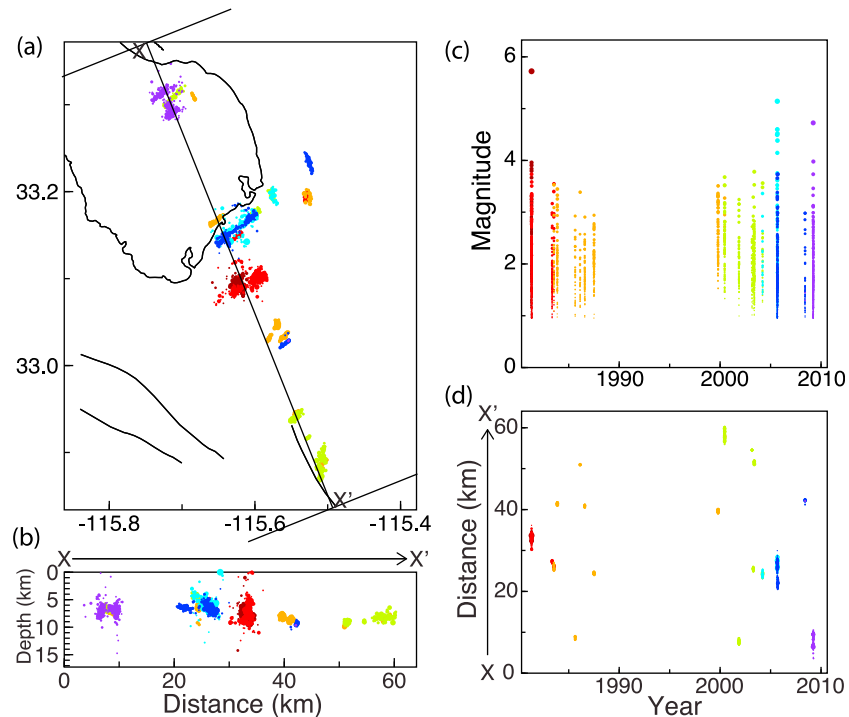
Figure 9. Seismic swarms in the Salton Trough. Events are colored by occurrence time with dark red indicating the earliest event and purple indicating the latest event. The size of the closed circles is assigned according to earthquake magnitude. (a) Map view of earthquake swarms, (b) cross-section view along profile X-X′ from Figure 9a, (c) magnitude versus time, (d) distance of earthquakes along X-X′ versus time.
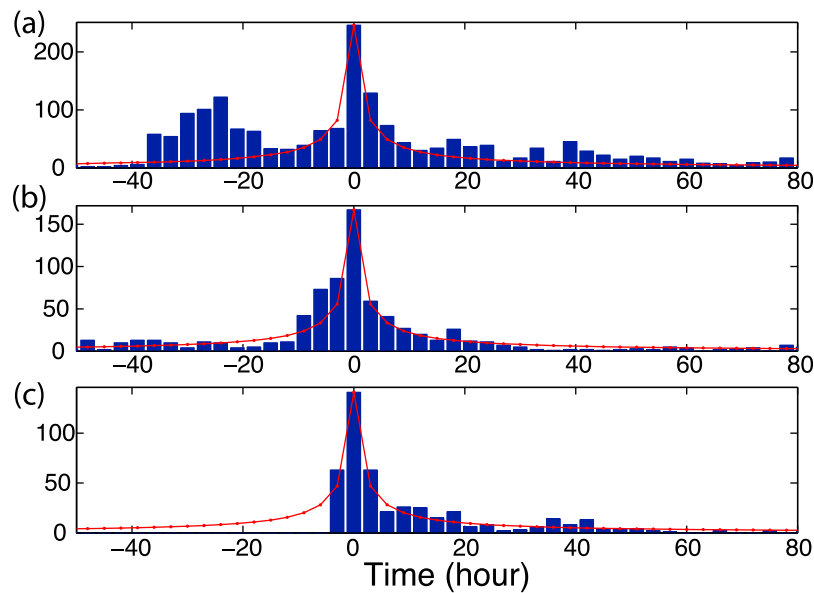
Figure 10. (a) Histograms of the stacked time histories for three swarms with more than 400 events within the late-M_{max} group, (b) eleven swarms with fewer than 200 events within the late-M_{max} group, and (c) early M_{max} group. Event time is relative to the largest event in each sequence. The red lines show the power law (t^{-1}) increase before the largest event and the decay after the largest event, i.e., Omori's Law.

Table 1. Information for Each Swarm[a]

Index	Starting Time	Location		Spatial Distribution			Duration (days)	t_{max}	Skew
		Latitude	Longitude	Strike	Dip	Shape			
1	04/20/1981, 18:49	33.095	−115.629	45.6	89.9	line	5.5	1.10	−9.36
1	04/25/1981, 04:01	33.097	−115.626	169.6	86.3	plane	5.5	1.10	−9.36
2	05/07/1983, 11:49	33.151	−115.623	52.2	87.1	plane	3.5	0.79	1.48
3	07/11/1983, 22:05	33.194	−115.527	165.4	87.5	sphere	2.2	0.86	−1.36
4	11/14/1983, 16:23	33.035	−115.559	41.4	87.2	line	0.6	0.79	0.97
5	08/20/1985, 16:23	33.306	−115.682	−26.3	86.4	line	0.07	0.65	0.67
6	02/17/1986, 09:35	32.946	−115.543	232.3	86.6	line	0.23	0.17	2.0
7	08/02/1986, 23:55	33.032	−115.579	27.3	85.6	line	1.0	2.23	0.22
8	06/28/1987, 10:56	33.164	−115.657	49.7	81.8	line	4.84	1.37	−0.38
9	10/18/1999, 20:32	33.047	−115.569	−11.7	78.9	sphere	0.49	0.08	−0.29
10	05/10/2000, 23:25	33.157	−115.636	179.7	81.2	plane	1.57	0.00	3.49
11	06/14/2000, 19:05	32.892	−115.506	184.2	70.8	plane	0.17	0.00	2.04
12	11/13/2001, 13:43	33.317	−115.703	43.4	87.3	plane	0.33	0.83	1.00
13	03/01/2003, 03:05	32.917	−115.528	227.9	82.5	line	0.23	0.71	−0.16
14	04/08/2003, 20:58	33.171	−115.603	42.9	76.7	line	5.12	0.78	1.12
15	05/23/2003, 15:39	32.937	−115.551	46.7	70.2	sphere	0.48	1.17	0.29
16	03/15/2004, 23:56	33.196	−115.577	−19.6	85.9	plane	0.04	0.30	2.83
17	08/31/2005, 09:32	33.176	−115.601	47.3	88.8	line	14.5	1.02	−0.34
17	09/01/2005, 10:24	33.147	−115.641	45.8	89.1	line	14.5	1.02	−0.34
18	09/15/2005, 0:57	33.242	−115.529	166.4	75.3	sphere	4.89	1.30	−0.59
19	06/02/2008, 02:30	33.028	−115.556	228.4	83.3	line	0.33	0.17	1.80
20	03/21/2009, 12:41	33.314	−115.725	57.0	83.3	plane	4.37	0.69	0.93
20	03/25/2009, 05:22	33.289	−115.716	48.9	85.5	line	4.37	0.69	0.93

[a]The spatial distribution is determined using an eigenvalue analysis (see text). The larger swarms (1981, 2005, 2009) divide naturally into subswarms, for which we show separate strikes and dips. We set the duration as the median of the time delay from the first event in the sequence.

angle shape. Thus we need to weight the misfit between predicted and observed times in a way that accounts for this behavior to obtain robust inversion results. We consider two types of migration:

$$\text{unilateral} : s_0\left(\vec{s} \cdot \left(\vec{X}_i - \vec{X}_0\right)\right) + t_0 = t_i \quad (5a)$$

$$\text{bilateral} : s_0\left|\vec{s} \cdot \left(\vec{X}_i - \vec{X}_0\right)\right| + t_0 = t_i \quad (5b)$$

in which s_0 is the migration slowness ($s_0 = 1/v_0$, where v_0 is velocity), $\vec{s}$ is the unit migration direction vector, $\vec{X}_i$ are the 3-D coordinates for each event, $\vec{X}_0$ is the starting location for migration, t_0 is the starting time of migration, and t_i is the occurrence time of each event. We use a grid search approach over θ, ϕ, $\vec{X}_0$, v_0, and t_0 to find the best fitting parameters (see Appendix A for details). To estimate the statistical significance of the migration and uncertainties for migration parameters, we use a bootstrap resampling method (see Appendix B).

[24] We find that most swarms migrate with probability greater than 95%, with a few having lower probabilities between 85% and 90%. The parameters θ and ϕ tend to trade off with each other since they are included in the inversion of the unit migration vector, so they usually have a larger variation range. A better approach is to estimate the total angular uncertainty in the migration directions, and the swarms usually have uncertainty estimates ranging from 10° to 20°. Migration modeling results for 20 swarms are listed in Table 2. The migration velocities range from 0.008 to 0.8 km/hour, with about 65% below 0.1 km/hour, lower than typical creep rates and aseismic slip rates [*Lohman and McGuire*, 2007; *Roland and McGuire*, 2009]. There is considerable scatter in plots of event time versus distance for individual swarms. To better show the overall migration

features, we combine results from all the swarms by plotting event time versus normalized distance (distance/v_0 where v_0 is the estimated migration velocity) in Figure 11a. Notice again the upper triangular nature of the migration behavior, in which activity continues for some time following its onset at a given location.

[25] The linear migration behavior is consistent with the assumption that aseismic slip (slow slip or creep) propagates along pre-fractured fault zones, modifies the localized stress field and triggers seismicity. However, as shown in Figure 5, some events are possibly induced seismicity from geothermal activities. The temporal distribution for the late-M_{max} group is also similar to swarms triggered by a fluid intrusion process [*Hainzl*, 2003]. Considering that swarms within the geothermal fields generally have migration velocities slower than typical aseismic slip rates, and their proximity to injection wells, it is possible that their migration behavior is controlled by fluid diffusion. In this case, instead of linear migration, the fluid-triggered seismicity front should follow the diffusion curve: $r = \sqrt{4\pi D t}$, where D is the diffusion coefficient and r is the distance for each event from the initiating point of fluid intrusion. The migration of induced seismicity away from injection wells has been used in different regions to estimate the hydraulic diffusion of the medium [*Audigane et al.*, 2002; *Shapiro et al.*, 2005].

[26] In order to explore possible fluid involvement, we find the best-fitting diffusion coefficient by modeling $r^2 = 4\pi D(t - t_0)$ using a similar fitting procedure to that used for linear migration. We also use a bootstrap approach to estimate the statistical significance of the migration parameters. We find four of the swarms, and the initial 100 hours for the swarm in 1981, are better fit with a diffusion curve than with linear migration. The results are listed in Table 3. Figure 11b shows event time versus normalized distance (i.e., divided by $\sqrt{4\pi D}$) for these four swarms and the fit of the diffusion

Table 2. Migration Parameter Estimates[a]

		Azimuth (deg)		Dip (deg)		Velocity (km/h)	
Index	Migration	Original	Range	Original	Range	Original	Range
1	100%, U	341.1	−71.6, 6.35	−65.9	−76.4, −55.8	0.024	0.021, 0.025
1	100%, U	155.5	132.0, 167.5	15.4	14.3, 23.4	0.071	0.065, 0.076
2	100%, U	246.0	208.2, 247.2	−62.5	−63.6, 2.82	0.015	0.013, 0.022
3	100%, U	10.9	8.6, 20.1	64.7	53.2, 71.6	0.039	0.023, 0.038
4	99%, U	204.8	199.0, 246.0	−1.8	−20.1, 13.1	0.058	0.046, 0.061
5	100%, U	330.8	−25.7, 10.9	−20.1	−33.8, −8.64	0.263	0.223, 0.333
6	86%, B	243.7	220.8, 243.6	47.5	45.2, 52.1	0.110	0.070, 0.128
7	94%, B	30.4	7.5, 41.9	75.0	59.4, 76.4	0.030	0.020, 0.044
8	100%, U	75.1	62.5, 79.7	−33.8	−48.7, −17.8	0.0079	0.007, 0.008
9	86%, U	195.6	156.6, 208.2	61.3	45.2, 83.0	0.090	0.060, 0.175
10	100%, U	1.76	−11.99, 15.52	13.1	9.12, 17.1	0.041	0.037, 0.045
11	100%, B	1.86	−2.35, 6.06	−7.5	−15.5, 9.7	0.338	0.307, 0.432
12	100%, U	204.8	193.3, 208.2	−0.62	−9.7, 10.7	0.367	0.274, 0.373
13	98%, B	59.1	45.4, 60.3	−55.6	−63.3, −52.7	0.091	0.078, 0.108
14	85%, U	41.9	25.8, 61.3	6.26	−6.35, 38.3	0.033	0.015, 0.036
15	98%, U	80.8	67.1, 80.8	23.4	−1.8, 33.8	0.150	0.114, 0.168
16	96%, U	138.3	130.3, 142.9	77.3	26.8, 84.2	0.856	0.645, 0.959
17	99%, U	200.2	196.7, 226.5	−22.4	−29.2, −6.35	0.134	0.117, 0.165
17	98%, U	210.5	208.2, 213.9	−32.7	−49.9, −36.1	0.089	0.077, 0.122
18	95%, U	133.7	129.1, 142.9	63.6	45.2, 76.8	0.080	0.079, 0.092
19	86%, U	234.6	199.1, 252.9	34.9	1.7, 47.5	0.316	0.193, 0.619
20	100%, B	62.5	54.6, 63.6	53.2	42.9, 53.3	0.015	0.015, 0.018
20	100%, B	41.9	42.0, 53.3	−40.7	−78.4., −34.9	0.036	0.035, 0.039

[a]"U" and "B" indicate the migration style: unilateral or bilateral. Each index corresponds to the same swarm in Table 1.

curve to the seismicity front. The estimated diffusion coefficients range from 0.2 to 0.6 m^2/s, within the range of values for reservoirs [*Shapiro et al.*, 2005]. The swarms are located within the Salton Sea and Brawley geothermal fields, close to geothermal wells, especially the three swarms that started shortly after nearby injection events. The physically reasonable diffusion coefficients we obtain and the timing related to injection activities suggest that fluid movement is involved in the propagation of seismicity.

6.4. Stress Drop and Migration

[27] As shown in Figures 7c and 8c, in some cases there is an increase of average stress drop with time as the swarm evolves. To find the relationship between stress drop and migration for other swarms, we divided events within each swarm into 8 bins with equal number of events, and found the median stress drop and time for each bin. The results exhibit a great deal of scatter and there is no clear trend of average stress drop with time. We also compared the stress drop values for swarm events with nearby non-swarm events but found no significant difference. Nonetheless, there are some variations in average stress drop among the different swarms. Swarms with migration velocities lower than 0.1 km/hour are mostly located within the lower stress drop regions, and their median stress drop is 0.25 MPa lower than swarms with faster migration velocities. This observation agrees with the results shown in Figure 6, since most of the slower migrating swarms are located within the Salton Sea geothermal field (see Figure 12), where stress drops are lower than average.

6.5. Migration and Tectonics

[28] The swarms are distributed in four distinct regions: (1) the southern end of the SAF (the newly discovered hinge zone that separates the Salton Sea into northern and southern sub-basins), (2) the southern shoreline of the Salton Sea (geothermal field), (3) the middle of the Brawley Seismic Zone (Brawley geothermal field), and (4) the northern end of the Imperial Fault (Mesquite basin). We refer to these regions by number in the following text. The major migration direction is NE-SW (around 45° ± 180°), and there are two swarms migrating at a faster velocity along the SAF parallel direction (NNW-SSE, around 145° ± 180°) (see Figure 12b).

[29] The general NE-SW direction changes from N60°E in region 4 to N30°E in region 1. The more northern trend in the Salton Sea was also noticed by *Brothers et al.* [2009]. The migration behaviors are different among the four clustered regions, which may be related to differences in material properties and the regional stress field. We plot the focal mechanism solutions from the SCSN (Southern California Seismic Network) moment tensor group and *Hardebeck and Shearer* [2003] to compare with the migration directions, shown in Figure 12. A parameter f_{type} from −1 (normal) to 0 (strike-slip) to 1 (reverse) is computed for each event based on the method of *Shearer et al.* [2006]. The majority of events involve strike-slip faulting, and the beach ball orientations generally agree with the migration direction in each region. Several normal faulting events are seen along the southern coast of the Salton Sea and the Mesquite Basin, consistent with the expected source mechanism for rapid subsidence regions.

[30] Region 1 marks the northern end of active extension and agrees with a hinge zone discovered by a seismic reflection survey [*Brothers et al.*, 2009]. The 2009 swarm exhibits complex migration behavior. It ruptured three parallel NE striking faults and the seismicity migrated both bilaterally along the NE direction at each fault and unilaterally along the NNW direction from the northernmost fault to the southernmost fault. The 2009 swarm is encompassed within a region of increased Coulomb stress resulting from the slip transient that occurred within the southern Salton
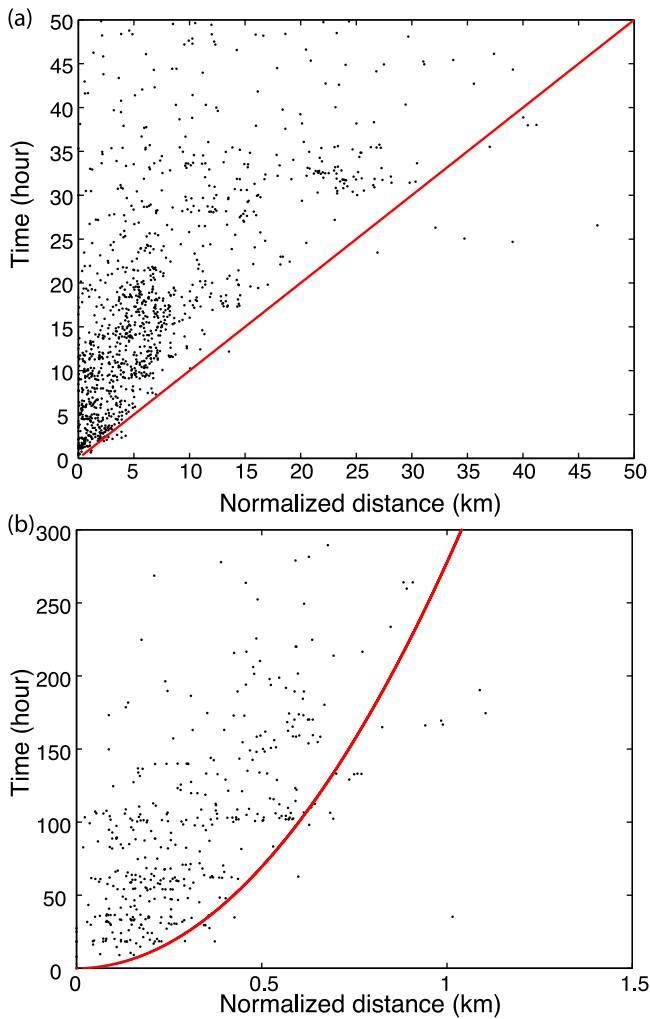
Figure 11. Stacked migration behavior of swarm seismicity. (a) A stacked linear migration curve for all swarms in Table 2, x axis is normalized distance by migration velocity. (b) A stacked diffusion curve for swarms in Table 3, x axis is normalized distance by $\sqrt{4\pi D}$ (D is the diffusion coefficient).

Sea from 2003 to 2009 [*Crowell et al.*, 2009], indicating an aseismic process is involved. The 2001 swarm unilaterally migrated along the NNE direction, which agrees with the fault plane of its largest event and the N15°E striking faults imaged during the seismic survey [*Brothers et al.*, 2009]. The 1985 swarm is confined to a narrow linear fracture zone and migrates along the SAF fault strike direction at a velocity around 0.3 km/hour, close to the propagation velocity of creep events and slow earthquake sequences on the SAF [*Linde et al.*, 1996; *King et al.*, 1973; *Burford*, 1977], and thus is most likely triggered by aseismic slip.

[31] The highest seismicity rate and most of the swarms occurred in region 2. Shown in Figures 5 and 6, as well as the diffusion modeling plotted in Figure 11b, the seismicity clustering and migration are at least partially controlled by geothermal injection/production activities. The NE-SW migrating swarms follow the first installation of geothermal injection wells in 1982, with average migration velocities

below 0.04 km/hour, which is about an order of magnitude lower than the reported creep events and historical large swarms [*Roland and McGuire*, 2009]. However, a swarm before the injection activities within this region did not exhibit migration behavior [*Gilpin and Lee*, 1978]. Similar movement was also found during a trilateration/GPS survey between 1987.95 and 1995.11, when increased injection and production were conducted. GPS stations located within the geothermal field moved significantly along a 250° azimuth, which is anomalous compared to the expected tectonic motion, suggesting it is caused by the geothermal wells located to the south and southwest [*Anderson et al.*, 2003]. Both the prior observations and geodetic measurements indicate that fluid diffusion may have a significant influence on the seismicity patterns.

[32] Although fluid diffusion is involved in the migration of swarms, the regional stress field resulting from the SAF-IF step-over is important. From Figure 12, the focal mechanism solutions for this region are primarily strike-slip faulting with several normal faulting events. Assuming the principal fault plane aligns with the NE-SW trend of seismicity and the overall NNW-SSE trending plate motion, the focal mechanisms indicate the NNW-SSE strike-slip faults are coupled by NE-SW left-lateral strike-slip faults, and the normal faulting accounts for extension between a series of parallel strike-slip faults. The overall swarm migration behavior in this region shows a similar pattern with NE-SW migrating swarms bounded by NNW-SSE migrating swarms, reflecting changes in the principal stress. A study of two seismic swarms in 1975 from a microearthquake survey prior to our analysis period reveals no migration of epicenters, with normal faulting striking N65°E for the larger swarm and strike-slip faulting for the smaller swarm with either N60°W for left-lateral motion or N30°E for right-lateral motion [*Gilpin and Lee*, 1978], consistent with the distribution in Figure 12.

[33] The swarm in 1981 bounds the NE-SW oriented faults and migrated at N30°W, parallel to the nearby strike-slip faults (see Figure 7). The seismicity started with a cluster of high stress drop events at depth and migrated upward during the initial 150 hours. Then a burst of low-stress drop events occurred, followed by along-strike migration and increasing stress drop. There is little spatial migration after the largest event occurred, possibly due to the coseismic deformation from the M 5.8 main shock. The temporal behavior of the seismicity exhibits two subclusters, each shows power law increasing and decreasing seismicity rate features (see Figure 10a). Such a migration pattern resembles seismicity triggered by a fluid intrusion process [*Hainzl and Fischer*, 2002]. After the initiation of seismicity, self-organized stress transfer and post-seismic creep among

Table 3. Hydraulic Diffusion Coefficient for Four Swarms[a]

Index	Date	Significance	Coefficient	Range
1	04/20/1981	100%	0.597	0.558, 0.631
2	05/07/1983	100%	0.446	0.419, 0.473
7	08/02/1986	94%	0.193	0.173, 0.213
8	06/28/1987	100%	0.279	0.211, 0.347
14	04/08/2003	100%	0.299	0.251, 0.347

[a]Range represents m²/s. Swarm index corresponds to index numbers in Table 1.
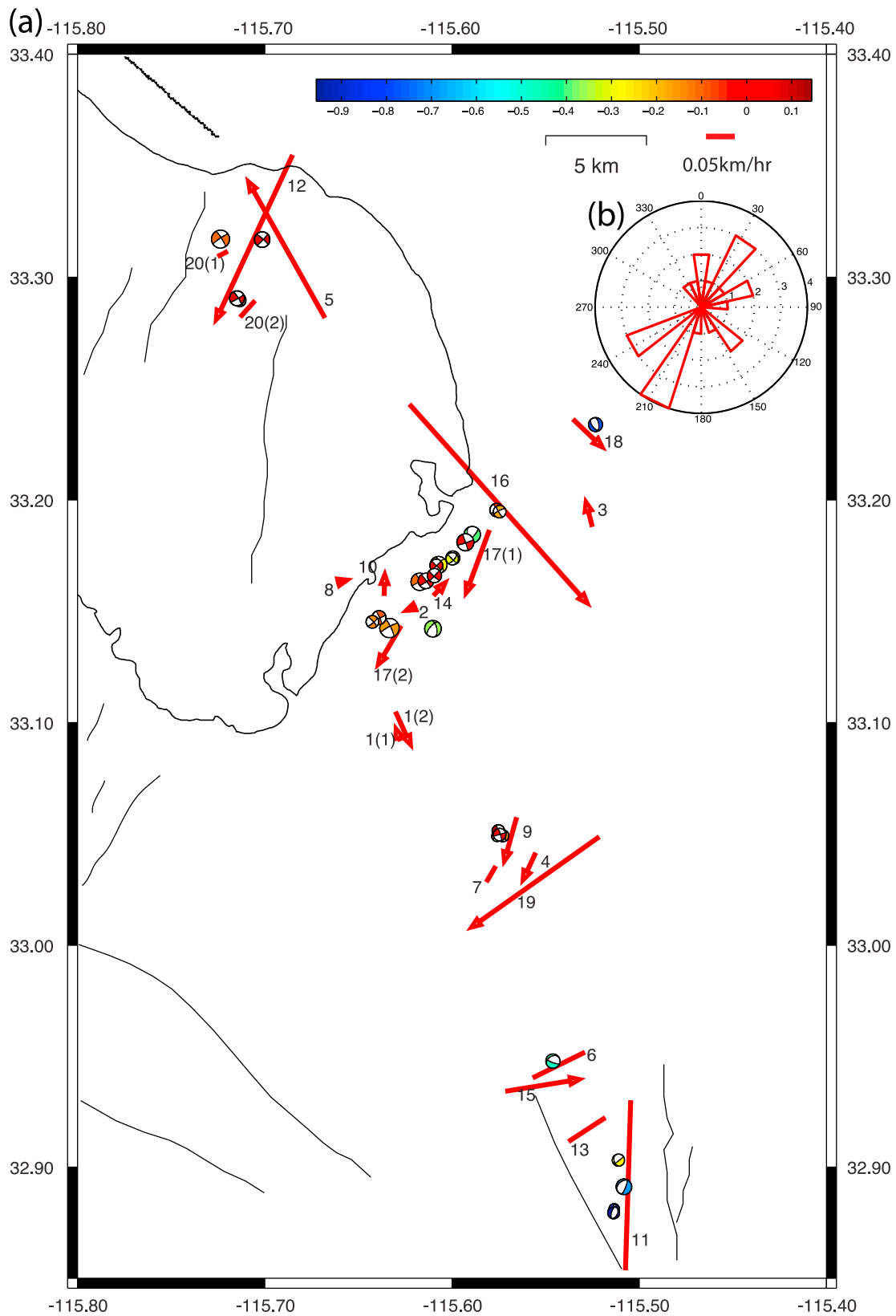
Figure 12. (a) Map view of swarm locations. The index numbers correspond to Table 1. Red lines with arrows show unilateral migration while red lines without arrows show bilateral migration. The length of each line is proportional to the migration velocity. The red line on the top right indicates a velocity of 0.05 km/hr. The beach balls are colored according to the type of focal mechanisms: −1 indicates normal faulting and 0 is strike-slip faulting. (b) Rose histogram of migration directions from Table 2.

successive events possibly drive the migration of the swarm [*Hainzl*, 2003, 2004].

[34] The large swarm in August, 2005 started less than 10 hours after a cluster of injection events, and exhibits NE-SW migration during the initial 10 hours (see Figure 8). However, the migration behavior is not clear after several magnitude 4 events occurred 10 hours later [see *Lohman and McGuire*, 2007, Figure 3]. Modeling with diffusion curves results in a larger misfit than linear migration, and the existence of aseismic slip has been confirmed by GPS and InSAR measurements [*Lohman and McGuire*, 2007; *Crowell et al.*, 2009]. The strain rate suddenly jumped in August 2005, which coincides with the high seismicity. Increased left-lateral motion is found along the N66°E Obsidian Buttes Fault (identified in a field survey), which coincides with the location and migration direction of the 2005 swarm [*Crowell et al.*, 2009]. The increased pore fluid pressure from multiple injection events prior to the seismicity may have contributed to bringing the fault to a critical failure point, while the aseismic slip is the major factor in driving the swarm seismicity.

[35] Region 3 is within the Brawley geothermal site and has low average stress drops, suggesting a weak region. Active exploration of geothermal energy lasted from 1983 to 1986, and the swarm occurring in 1986 exhibits apparent diffusion migration, possibly due to the increased fluids during the injection period. Three swarms in 1983, 1986 and 2008 show consistent fault planes striking NE-SW, which generally agrees with the preferred extensional stress orientation resulting from the step-over between the San Andreas and Imperial faults. The 1999 swarm occurred along a NNW striking fault plane. However, all the swarms exhibit consistent migration directions, indicating the regional stress field is controlling the migration. The migration velocities are between 0.06 and 0.4 km/hour, within the range of nearby creep events and aseismic slip driven swarms [*Lohman and McGuire*, 2007; *Roland and McGuire*, 2009].

[36] The focal mechanisms show that the Mesquite Basin is actively subsiding and the swarm in 2000 probably marks the southern limit for this basin. This region is seismically active, and four swarms are identified during our study period. Three swarms show consistent migration directions approximately N50°E, and locate at the northern boundary of the seismicity. Their location and orientation are consistent with the northern boundary fault of the swarm in 1975 [*Johnson and Hadley*, 1976]. The 2000 swarm is further south on the Imperial Fault and migrates bilaterally along a NS direction at 0.4 km/hour. Both the velocity and migration direction are similar to the beginning of the swarm in 1975 [*Johnson and Hadley*, 1976], suggesting the four swarms are triggered by a similar process to that of the swarm in 1975. The Brawley fault is proposed to explain the overall NNW trend of the Brawley Seismic Zone, and the swarm in 1975 ruptured the Brawley fault. The NE northern boundary fault accommodates the extension between the Imperial Fault and the Brawley Fault [*Hill et al.*, 1975; *Johnson and Hadley*, 1976]. The swarms in the Mesquite Basin have migration behavior that cannot be modeled as fluid diffusion, and the velocities ranging from 0.1 to 0.4 km/hour are consistent with the observed slow slip event propagation velocity of 0.14 km/hour from creep meters in the southern Imperial Fault zone [*Glowacka et al.*, 2001].

Thus the slow slip events are the best explanation for the observed swarm migration behavior in this region.

7. Discussion

[37] Our Brune-type stress drop estimates depend upon the assumed source model and care should be taken in comparing the absolute stress drop values with those of other studies, which may have made different modeling assumptions. However, our results can be compared with other stress drops in Southern California and Parkfield, which were calculated using the same method [*Shearer et al.*, 2006; *Allmann and Shearer*, 2007]. The average stress drop of 0.56 MPa is similar to the estimates of *Shearer et al.* [2006], significantly lower than the rest of Southern California and the Parkfield section. High heat flow in the Salton Trough is a likely cause as other studies also observe relatively low stress drops within geothermal areas, i.e., the Coso geothermal field and triggered earthquakes within the Salton Sea geothermal field [*Hough et al.*, 1999; *Hough and Kanamori*, 2002]. Analysis of spatial variations of stress drop within the Salton Trough shows the median stress drop within geothermal fields is 0.12 MPa lower than other areas. We observe increasing median stress drop with distance from injection wells up to 2.5 km away. Using the median wellhead pressure of 1 Mpa, constant pressure for 30 days (the median duration of injection events), and assuming a diffusion coefficient of 0.25 m^2/s, we calculate the pore pressure perturbation using the method of *Dinske and Shapiro* [2010]. We obtain roughly a 0.02 MPa pore pressure change 0.05 km away and about a 0.001 MPa change 0.6 km away by the end of the injection event, and the perturbation drops rapidly at greater distance. The perturbation beyond 1 km based on this simple calculation for a single injection event is too low to account for the stress drop variations. There are usually multiple injection events occurring around the same time at different locations (see Figure 8c) and it is possible that the combined fluid level and pressure perturbations would have a greater impact.

[38] Induced seismicity has been well documented and studied in the Geysers geothermal field [e.g., *Majer et al.*, 2007], where there is a general long-term temporal correlation between water injection and seismicity. Figures 5b and 5c show a correlation of increased seismicity with injection activities within local clusters. To check this relationship over a longer time span than the LSH catalog and to examine the seismicity rate before and after injection events began in 1982, we use the un-relocated SCEC catalog to obtain additional events between 1933 and 1981. We only consider events with magnitudes larger than 3 to account for the low magnitude completeness level for the older parts of the catalog. As shown in Figure 13b, the seismicity within the Salton Sea geothermal field remained at a low level before the injection started, and increased significantly (by approximately six times) after that. The Bombay Beach region is generally seismically quiet until the 2001 and 2009 swarms. Within the northern Imperial Fault and the Brawley Seismic Zone, the seismicity is dominated by periodic seismic bursts, with the highest seismicity rate during the aftershock sequence of the 1979 Mw 6.4 Imperial Valley earthquake, and a relatively quiet period after that. The changes of long-term seismicity rate indicate that seismicity
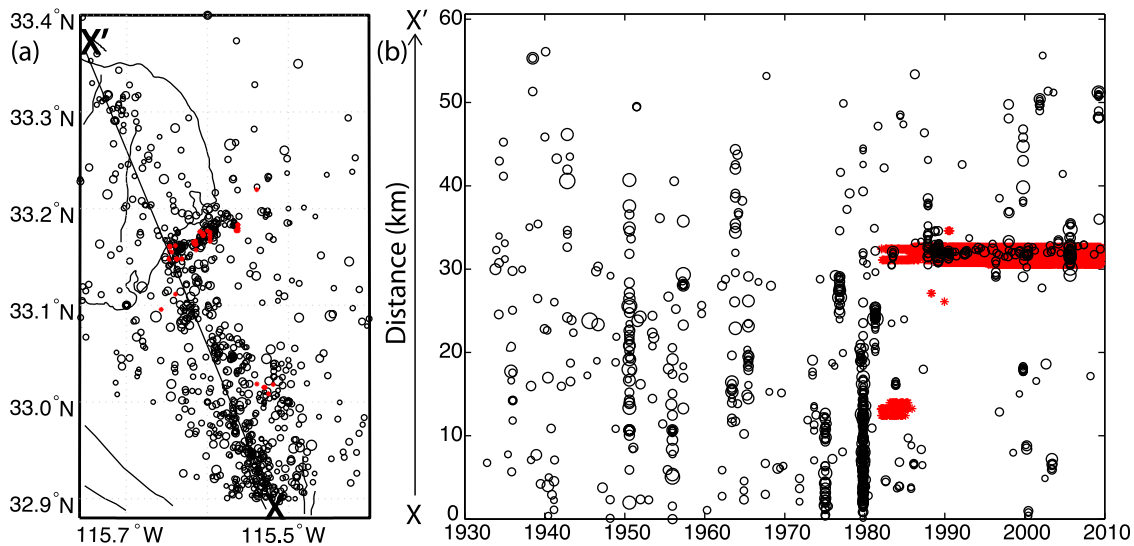
Figure 13. (a) Map view of earthquakes with $M \geq 3$ since 1933. The size of the black circles scale according to the size of the event. Red stars are the injection well locations. (b) Distance along profile X-X′ versus time for earthquakes (black circles) and injection event (red stars).

events within the Salton Sea geothermal field are strongly influenced by geothermal activities, while tectonic stress accumulation is the dominant effect in other regions within the Salton Trough. The difference is also suggested in the earthquake swarm migration behavior.

[39] Using similar criteria as *Vidale and Shearer* [2006], we identified 20 distinct seismic bursts. Analysis of the temporal and spatial distribution of these bursts indicates they all have low seismic moment skew values and spatial migration behavior with a statistical significance greater than 85%. Therefore, despite differences in the timing of their largest event, we consider all of the bursts to be swarms rather than main shock-aftershock sequences. Modeling of the seismicity front shows that the migration directions are generally consistent among local areas. Several of the swarms are better-fit with a diffusion curve than a linear migration velocity. These swarms are mostly located within the Salton Sea geothermal field, and three may have been triggered by nearby injection events. The swarm located within the Brawley geothermal field occurred around the end of the injection period when fluid levels may have been greatest. The previous observed creep rates and aseismic slip rates within this region are between 0.1 and 0.4 km/hour [*Roland and McGuire*, 2009], which are about an order of magnitude higher than the migration velocities within the Salton Sea geothermal field, but agree with the estimated migration rates for other regions. The observed migration behavior also suggests differences among the driving force for swarms within different areas, with fluid diffusion involved in the geothermal field and slow slip or creep events involved for the other swarms.

8. Conclusion

[40] Analysis of the source spectra for 3332 earthquakes in the Salton Trough from 1981 to 2009 with a multiple-event EGF method reveals variations in both attenuation and stress drop. Estimated lateral variations in attenuation

involve Δt^* values from -0.006 to 0.008 s, with higher attenuation within subsidence basins. Computed Brune-type stress drops range from 0.1 to 3.7 MPa with a median value of 0.56 MPa. The stress drops are much lower than most regions in Southern California. Lower stress drops are observed within the geothermal fields and a dependence on distance from injection well locations is suggested. Detailed analysis shows that the geothermal activities strongly influence the seismicity within the Salton Sea geothermal field. 20 distinct swarms are identified from the precisely relocated catalog. The swarms may be divided into two groups, depending upon the relative timing of their largest event. A power law decay of seismicity rate after the largest event is observed for all groups, while a power law increase is seen building up to the largest event for the late-$M_{\max}$ group. Two subclusters are seen for the three large swarms within the late-$M_{\max}$ group. Consistent swarm migration directions are observed within each local area. Estimated swarm migration velocities range from 0.008 to 0.8 km/hour, and diffusion coefficients range from 0.2 to 0.6 m^2/s. Slow tectonic slip events are a likely driving mechanism for most of the swarms, but fluid diffusion may also drive swarms within the active geothermal fields.

Appendix A: Migration Modeling

[41] We develop a weighted L1-norm method to find the best-fitting migration vector, using the parameterizations in Equations 5a and 5b. We use a grid search approach over θ, ϕ (negative for upward migration), $\vec{X}_0$, v_0, and t_0 to find the best fitting parameters:

[42] 1. For each azimuth θ from 0 to 2π, and vertical angle ϕ from $-\frac{\pi}{2}$ to $\frac{\pi}{2}$ (for bilateral migration), we calculate the migration vector:

$$\vec{s} = \begin{cases} \cos\phi\cos\theta \\ \cos\phi\sin\theta \\ \sin\phi \end{cases} \quad (A1)$$

[43] 2. Using the migration vector, we find the starting location $\vec{X}_0$ for bilateral migration by grid searching the 3-D coordinates over the swarm region. For unilateral migration, the starting location trades off with t_0, so we set $\vec{X}_0$ as the location for the first event.

[44] 3. The distance along the migration direction is $D_i = \vec{s} \cdot (\vec{X}_i - \vec{X}_0)$. We loop over possible velocities by finding an initial velocity from the interquartile range of distance and time, then set the interval as $dv = 0.1 \times \log_{10}(v_0)$ (max(dv) = 0.01, units are km/hour). In this way, we have different ranges for velocities at different levels, which increases the efficiency of the search.

[45] 4. At each possible v_0, we set $t_0 = 0$, calculate t_i^p from equations (5a) and (5b), then set $dt_i = t_i - t_i^p$. We find t_0 from min(dt_i) to max(dt_i) which can minimize $\sum w_i \times |dt_i - t_0|$, where the weight w_i is defined as

$$w_i = \begin{cases} |dt_i - t_0|; & (dt_i - t_0) < 0 \\ 1; & (0 \leqslant dt_i - t_0 < 0.5) \\ 1/\sqrt{(dt_i - t_0)}; & (dt_i - t_0 \geqslant 0.5) \end{cases} \quad (A2)$$

This weighting approach accounts for the upper-triangular nature of the time versus distance behavior by applying the L1-norm only within a 1/2 hour window, and penalizing earlier arrivals more than late arrivals outside of this window.

[46] 5. Update $dt_i^{new} = dt_i - t_0$, then using the same weighting procedure, find the combination of parameters that minimizes $\sum w_i^{new} \times |dt_i^{new}|$.

[47] Applying this method to the Salton swarm sequences produces results that generally agree with the trends that can be seen from visual inspection. For a swarm on 03/15/2004, which only lasted about 2 hours, the duration is too short for the inversion method to obtain a reliable result. Instead of solving for t_0, we find that setting t_0 to the time of the first event gives the best result for this swarm.

[48] For diffusion curve modeling, the migration follows: $r = \sqrt{4\pi D t}$, where D is the diffusion coefficient and r is the distance for each event from the location of fluid intrusion. For convenience, we model $r^2 = 4\pi D(t - t_0)$ using the linear method, in which $r^2 = |X - X_0|^2$. We apply a similar grid search method and weighing procedure to find the best-fitting diffusion coefficient and misfit for the true data set.

Appendix B: Statistical Tests

[49] We perform two statistical tests for the significance of our swarm migration parameters. We first check whether we obtain a significantly better fit to the data than what might be expected by random chance. For this test, we randomly scramble (shuffle) the occurrence times for the events in the swarm, but keep their true locations. In this way, all actual time migration behavior is removed. Then we run the inversion process for the new set of data, and calculate the best-fitting parameters and resulting misfit. This process is repeated 100 times, and we estimate the probability that migration is resolved as the fraction of times the true data set produces a lower misfit than the time-scrambled data sets. With this method, we find that most swarms migrate with probability greater than 95%, with a few having lower probabilities between 85% and 90%.

[50] The second test is to estimate confidence limits for the migration parameters using a bootstrap resampling method. We treat the time and location for each event as a 4-D data set $X(x_i, y_i, z_i, t_i, i = 1....N)$, and randomly resample the data set by generating the random integer sequence $I(i_i, i = 1....N)$ and a new data set $X_n = X(x_k, y_k, z_k, t_k, k = i_i, i = 1....N)$. A new set of best-fitting parameters is solved for each new data set, and the range is found from 100 separate resampling results. Tests of this approach applied to the synthetic data set show that the estimated dip angle will generally have a larger uncertainty than the azimuth. The parameters θ and ϕ tend to trade off with each other since they are included in the inversion of the unit migration vector, so they usually have a larger range. A better approach is to estimate the total angular uncertainty in the migration directions, which generally produces uncertainty estimates for the real data set of 10° to 20°.

[51] For the diffusion modeling, we apply the same bootstrap procedure to find the migration significance and estimated uncertainties in the diffusion coefficient. To determine whether we obtain a better with a diffusion curve, we apply the second bootstrap test for the same data set with both linear migration and the diffusion curve with 100 times resampling. Then we use the cumulative density function to compare the misfit distributions from the two migrations, and check if the diffusion curve has a lower misfit than the linear migration. The five data sets with lower misfits using the diffusion curve are listed in Table 3.

References

Allmann, B. P., and P. M. Shearer (2007), Spatial and temporal stress drop variations in small earthquakes near Parkfield, California, *J. Geophys. Res.*, *112*, B04305, doi:10.1029/2006JB004395.

Anderson, G., D. C. Agnew, and H. O. Johnson (2003), Salton trough regional deformation estimated from combined trilateration and survery-mode GPS data, *Bull. Seismol. Soc. Am.*, *93*, 2402–2414.

Audigane, P., J. J. Royer, and H. Kaieda (2002), Permeability characterization of the Soultz and Ogachi large-scale reservoir using induced seismicity, *Geophysics*, *67*(1), 204–211.

Båth, M. (1965), Lateral inhomogeneities of the upper mantle, *Tectonophysics*, *2*(6), 483–514.

Brothers, D. S., N. W. Driscoll, G. M. Kent, A. J. Harding, J. M. Babcock, and R. L. Baskin (2009), Tectonic evolution of the Salton Sea inferred from seismic reflection data, *Nat. Geosci.*, *2*(8), 581–584.

Brune, J. N. (1970), Tectonic stress and the spectra of seismic shear waves from earthquakes, *J. Geophys. Res.*, *75*, 4997–5009.

Burford, R. O. (1977), Bimodal distribution of creep event amplitudes on the San Andreas fault, California, *Nature*, *268*, 424–426.

Crowell, B. W., Y. Bock, and D. T. Sandwell (2009), Interseismic strain accumulation in the imperial valley and implications for triggering of large earthquakes in Southern California, *Eos Trans. AGU*, *90*(54), Fall Meet. Suppl., Abstract T33E-02.

Dinske, C., and S. Shapiro (2010), Interpretation of microseismicity induced by time-dependent injection pressure, *SEG Expanded Abstr.*, *29*, 2125–2129.

Enescu, B., S. Hainzl, and Y. Ben-Zion (2009), Correlations of seismicity patterns in southern California with surface heat flow data, *Bull. Seismol. Soc. Am.*, *99*, 3114–3123.

Farrell, J., S. Husen, and R. B. Smith (2009), Earthquake swarm and b-value characterization of the Yellowstone volcano-tectonic system, *J. Volcanol. Geotherm. Res.*, *188*(1–3), 260–276.

Fischer, T. (2003), The August-December 2000 earthquake swarm in NW Bohemia: The first results based on automatic processing of seismograms, *J. Geodyn.*, *35*(1–2), 59–81.

Gilpin, B., and T. C. Lee (1978), Micro-earthquake study in Salton Sea geothermal area, California, *Bull. Seismol. Soc. Am.*, *68*, 441–450.

Glowacka, E., J. J. Gonzalez, F. A. Nava, F. Farfan, and G. Diaz de Cossio (2001), Monitoring surface deformation in the Mexicali Valley, BC, Mexico, paper presented at 10th FIG International Symposium on Deformation Measurements, Calif. Inst. of Technol., Organe.

Goertz-Allmann, B. P., A. Goertz, and S. Wiemer (2011), Stress drop variations of induced earthquakes at the Basel geothermal site, *Geophys. Res. Lett.*, *38*, L09308, doi:10.1029/2011GL047498.

Goldsmith, M. (1976), Geothermal development and the Salton Sea, *Energy*, *1*, 367–373.

Gunasekera, R. C., G. R. Foulger, and B. R. Julian (2003), Reservoir depletion at the Geysers geothermal area, California, shown by four-dimensional seismic tomography, *J. Geophys. Res.*, *108*(B3), 2134, doi:10.1029/2001JB000638.

Hainzl, S. (2003), Self-organization of earthquake swarms, *J. Geodyn.*, *35*(1–2), 157–172.

Hainzl, S. (2004), Seismicity patterns of earthquake swarms due to fluid intrusion and stress triggering, *Geophys. J. Int.*, *159*(3), 1090–1096.

Hainzl, S., and T. Fischer (2002), Indications for a successively triggered rupture growth underlying the 2000 earthquake swarm in Vogtland/NW Bohemia, *J. Geophys. Res.*, *107*(B12), 2338, doi:10.1029/2002JB001865.

Hainzl, S., and Y. Ogata (2005), Detecting fluid signals in seismicity data through statistical earthquake modeling, *J. Geophys. Res.*, *110*, B05S07, doi:10.1029/2004JB003247.

Hardebeck, J. L., and P. M. Shearer (2003), Using S/P amplitude ratios to constrain the focal mechanisms of small earthquakes, *Bull. Seismol. Soc. Am.*, *93*, 2434–2444.

Hauksson, E., and P. M. Shearer (2006), Attenuation models (Q_p and Q_s) in three dimensions of the southern California crust: Inferred fluid saturation at seismogenic depths, *J. Geophys. Res.*, *93*, B05302, doi:10.1029/2005JB003947.

Hayashi, Y., and Y. Morita (2003), An image of a magma intrusion process inferred from precise hypocentral migrations of the earthquake east of the Izu peninsula, *Geophys. J. Int.*, *153*(1), 159–174.

Hill, D. P., P. Mowinckel, and L. G. Peake (1975), Earthquake, active faults, and geothermal areas in the Imperial Valley, California, *Science*, *188*, 1306–1308.

Hough, S. E., J. M. Lees, and F. Monastero (1999), Attenuation and source properties at the Coso geothermal area, California, *Bull. Seismol. Soc. Am.*, *89*, 1606–1619.

Hough, S. E., and H. Kanamori (2002), Source properties of earthquakes near the Salton Sea triggered by the 16 October 1999 M 7.1 Hector Mine, California, earthquake, *Bull. Seismol. Soc. Am.*, *92*, 1281–1289.

Johnson, C. E., and D. M. Hadley (1976), Tectonic implications of Brawley earthquake swarm, Imperial-Valley, California, January 1975, *Bull. Seismol. Soc. Am.*, *66*, 1133–1144.

Kanamori, H. (1977), The energy release in great earthquakes, *J. Geophys. Res.*, *82*, 2981–2987.

King, C. Y., R. D. Nason, and D. Tocher (1973), Kinematics of fault creep, *Philos. Trans. R. Soc. A.*, *274*, 344–360.

Lin, G., P. M. Shearer, E. Hauksson, and C. H. Thurber (2007a), A three-dimensional crustal seismic velocity model for southern California from a composite event method, *J. Geophys. Res.*, *112*, B11306, doi:10.1029/2007JB004977.

Lin, G., P. Shearer, and E. Hauksson (2007b), Applying a three-dimensional velocity model, waveform cross correlation, and cluster analysis to locate southern California seismicity from 1981 to 2005, *J. Geophys. Res.*, *112*, B12309, doi:10.1029/2007JB004986.

Linde, A. T., M. T. Gladwin, M. J. S. Johnston, R. L. Gwyther, and R. G. Bilham (1996), A slow earthquake sequence on the San Andreas fault, *Nature*, *383*, 65–68.

Lohman, R. B., and J. J. McGuire (2007), Earthquake swarms driven by aseismic creep in the Salton Trough, California, *J. Geophys. Res.*, *112*, B04405, doi:10.1029/2006JB004596.

Madariaga, R. (1976), Dynamics of an expanding circular fault, *Bull. Seismol. Soc. Am.*, *66*, 639–666.

Majer, E. L., R. Baria, M. Stark, S. Oates, J. Bommer, B. Smith, and H. Asanuma (2007), Induced seismicity associated with enhanced geothermal systems, *Geothermics*, *36*(3), 185–222.

Ogata, Y. (1988), Statistical models for earthquake occurrences and residual analysis for point-processes, *J. Am. Statist. Assoc.*, *83*, 9–27.

Omori, F. (1895), On the aftershocks of earthquakes, *J. Coll. Sci. Imp. Univ. Tokyo*, *7*, 111–200.

Roland, E., and J. J. McGuire (2009), Earthquake swarms on transform faults, *Geophys. J. Int.*, *178*(3), 1677–1690.

Ross, A., G. R. Foulger, and B. R. Julian (1999), Source processes of industrially-induced earthquakes at the Geysers geothermal area, California, *Geophysics*, *64*(6), 1877–1889.

Schlotterbeck, B. A., and G. A. Abers (2001), Three-dimensional attenuation variations in southern California, *J. Geophys. Res.*, *106*, 30,719–30,735.

Schmitt, A. K., and J. B. Hulen (2008), Buried rhyolites within the active, high-temperature Salton Sea geothermal system, *J. Volcanol. Geotherm. Res.*, *178*(4), 708–718.

Shapiro, S. A., S. Rentsch, and E. Rothert (2005), Characterization of hydraulic properties of rocks using probability of fluid-induced microearthquakes, *Geophysics*, *70*(2), F27–F33.

Shearer, P. M., G. A. Prieto, and E. Hauksson (2006), Comprehensive analysis of earthquake source spectra in southern California, *J. Geophys. Res.*, *111*, B06303, doi:10.1029/2005JB003979.

Svensen, H., Ø. Hammer, A. Mazzini, N. Onderdonk, S. Polteau, S. Planke, and Y. Y. Podladchikov (2009), Dynamics of hydrothermal seeps from the Salton Sea geothermal system (California, USA) constrained by temperature monitoring and time series analysis, *J. Geophys. Res.*, *114*, B09201, doi:10.1029/2008JB006247.

Vidale, J. E., and P. M. Shearer (2006), A survey of 71 earthquake bursts across southern California: Exploring the role of pore fluid pressure fluctuations and aseismic slip as drivers, *J. Geophys. Res.*, *111*, B05312, doi:10.1029/2005JB004034.

X. Chen and P. M. Shearer, Scripps Institution of Oceanography, University of California, San Diego, La Jolla, CA 92093, USA. (xic002@ucsd.edu)